



# **Geophysical Research Letters**°

# **RESEARCH LETTER**

10.1029/2021GL097319

#### **Key Points:**

- We estimated T<sub>ex</sub>, a residence time of rock masses on hillslopes beyond threshold angles, as ~61-157 kyr in the eastern Tibetan mountains
- T<sub>ex</sub> increases with slope and is similar across lithologies, but slightly longer for metamorphic rocks
- T<sub>ex</sub> represents the construction and decay time scales of excess topography, which is ~3–9% of rejuvenation time scale for topographic relief

#### **Supporting Information:**

Supporting Information may be found in the online version of this article.

#### Correspondence to:

G. K. Li and S. Moon, ligen@ucsb.edu; sgmoon@epss.ucla.edu

#### Citation:

Li, G. K., Moon, S., & Higa, J. T. (2022). Residence time of over-steepened rock masses in an active mountain range. *Geophysical Research Letters*, 49, e2021GL097319. https://doi.org/10.1029/2021GL097319

Received 3 DEC 2021 Accepted 15 MAR 2022

# Residence Time of Over-Steepened Rock Masses in an Active Mountain Range

Gen K. Li<sup>1,2</sup>, Seulgi Moon<sup>1</sup>, and Justin T. Higa<sup>1</sup>

<sup>1</sup>Department of Earth, Planetary, and Space Sciences, University of California, Los Angeles, CA, USA, <sup>2</sup>Department of Earth Science, University of California, Santa Barbara, CA, USA

**Abstract** In uplifting mountains, hillslopes steepen toward a threshold angle set by substrate material strength. Hillslopes beyond the threshold angle, referred to as excess topography, are mechanically unstable. The residence time scale of rock masses in excess topography ( $T_{ex}$ ) is critical for understanding time scales of surface processes and landscape evolution in steep mountains. However,  $T_{ex}$  remains loosely constrained for varying slopes and lithologies. Here, we calculate  $T_{ex}$  in the eastern Tibetan mountains by quantifying excess topography across lithologies, long-term landslide erosion rates caused by seismicity and climate, and exhumation rates.  $T_{ex}$  increases with local slope angles and is of the same order of magnitude across different lithologies but slightly longer for metamorphic rocks. Range-scale  $T_{ex}$  is estimated as  $\sim$ 61–157 kyr,  $\sim$ 3–9% of the relief-rejuvenation timespan of threshold topography. Similar  $T_{ex}$  regardless of lithologies and methods suggest steady-state construction and erosion of excess topography over thousand to million years time scales in this orogen.

Plain Language Summary High relief and steep slopes are characteristic of mountainous landscapes. Hillslopes become unstable once their gradients exceed a critical angle set by hillslope material strength. Rock masses residing on hillslopes steeper than the critical angle are prone to landslide failures, representing a major hazard and primary agent of erosion. To better understand the lifespan of unstable rock masses, we quantify how long these masses can reside on over-steepened parts of hillslopes in eastern Tibetan mountains as a case study. We estimate an average residence time of ~61–157 thousand years for rock masses on over-steepened slopes. This residence time is consistent using both landslide erosion rates over thousands of years and exhumation rates over millions of years. Rock masses on steeper slopes seem to have a longer residence time than those on shallower slopes. Residence times are also similar across varying rock types, slightly longer for metamorphic rocks. Our estimated residence time scale represents ~3–9% of the estimated timespan needed for hillslopes to grow and steepen beyond the critical angle, which helps to evaluate the construction and destruction time scales of unstable rock masses.

### 1. Introduction

In active mountain ranges, tectonic uplift and channel incision steepen hillslopes toward a threshold angle (Bennett et al., 2016; Burbank et al., 1996; Larsen & Montgomery, 2012; Montgomery, 2001). Approaching this angle, hillslopes respond to increases in uplift rates by nonlinearly increasing landslide erosion rates rather than steepening their gradients (Larsen & Montgomery, 2012). This theoretical model of "threshold landscapes" is supported by observations of modal hillslope angles ~30–40°, comparable to typical friction angles that are set by the strength of substrate materials (Montgomery, 2001). Previous studies have shown that threshold landscapes exist in multiple orogens (e.g., the Himalayas, eastern Tibet, and New Zealand; Burbank et al., 1996; Korup, 2008; Ouimet et al., 2009; Whipple et al., 1999).

Although mean slope angles from these landscapes are close to common friction angles, a significant proportion of hillslopes are steeper than threshold angles (Montgomery et al., 2001). Blöthe et al. (2015) termed these over-steepened hillslopes "excess topography" and developed an algorithm to quantify unstable rock-mass volumes in excess topography. Rock masses in excess topography are mechanically unstable and prone to failure (Blöthe et al., 2015; Montgomery, 2001). Landslides from these unstable rock masses regulate landscape evolution and sediment and carbon fluxes (Croissant et al., 2021; Emberson et al., 2016; Korup, 2007; Marc et al., 2019), making excess topography a nexus between tectonics, climate, and surface processes.

© 2022. American Geophysical Union. All Rights Reserved.

LI ET AL. 1 of 10



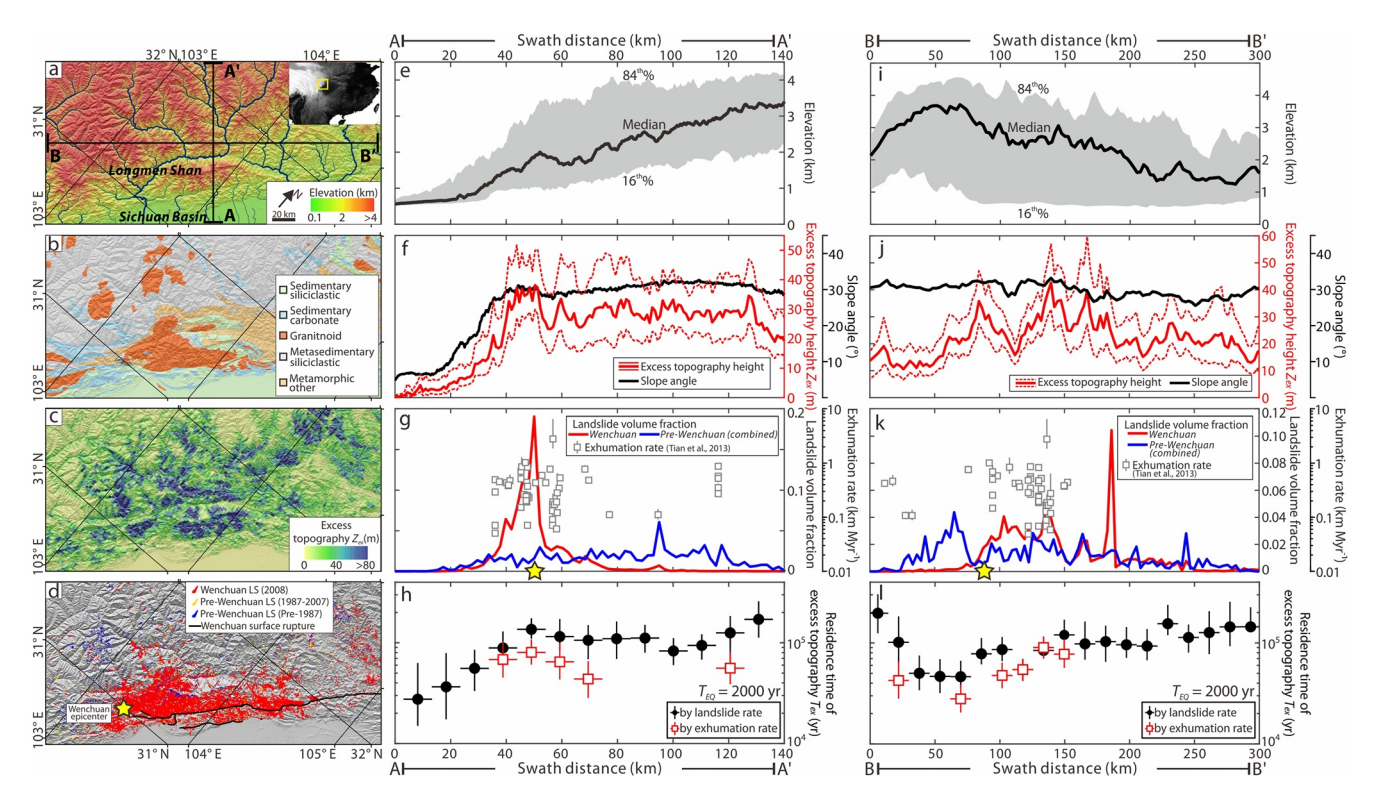


Figure 1. Maps and swath profiles of topography, erosion rates, and  $T_{ex}$  of the Longmen Shan. Maps of (a) elevation, (b) geology (Ye et al., 2017), (c) mean height of excess topography ( $Z_{ex}$ ) calculated in 1 × 1 km grids, and (d) the Wenchuan and pre-Wenchuan landslide inventories with the surface rupture and epicenter of the Wenchuan earthquake (Liu-Zeng et al., 2009) are shown. Swath profiles along (e-h) A-A' and (i-l) B-B' shown in (a) are for (e, i) elevation (black: median, gray: 16th-84th percentiles), (f, j)  $Z_{ex}$  (red solid and dashed curves: mean  $\pm$  1 $\sigma$ ) and slope angle (black curve: median), (g, k) landslide volume fractions and locations of exhumation rate data (error bars:  $\pm$ 1 $\sigma$  errors, only displaying data from excess topography using  $\theta_{L0}$ ); (h, l)  $T_{ex}$  (filled black circles: landslide-derived  $T_{ex}$  based on  $\theta_{L0}$  with error bars from  $\theta_{Llow}$  and  $\theta_{Lup}$ , open red squares: exhumation-derived  $T_{ex}$  based on  $\theta_{L0}$ ). Calculations are based on (e-g, i-k) 2-km, (h) 10-km, and (l) 15-km intervals along transects.

The residence time scale of rock masses in excess topography (hereafter,  $T_{ex}$ ) is determined as:

$$T_{ex} = V_{ex} / (e \times A_{ex}) \tag{1}$$

where  $V_{ex}$  is the rock-mass volume in excess topography (km³), e is the erosion rate of a rock mass in excess topography (mm yr $^{-1}$ ), and  $A_{ex}$  is the area over which  $V_{ex}$  is estimated (km $^2$ ).  $T_{ex}$  essentially calculates a turnover time of  $V_{ex}$ , which is equivalent to a residence time under steady state (Bolin & Rodhe, 1973). Understanding  $T_{ex}$  is critical for evaluating the status and time scale of landscape evolution in uplifting mountains. However,  $T_{ex}$  still remains loosely constrained for steep landscapes with mixed lithologies, and it is unclear how  $T_{ex}$  varies with slope and lithology.

In this work, we quantify  $V_{ex}$  and  $T_{ex}$  in the eastern Tibetan mountains. Previous studies have characterized geology, topography, rock uplift, and erosion in this region, laying the foundation for our study (e.g., Kirby et al., 2003; Liu-Zeng et al., 2011; Ouimet et al., 2009). Here, we first calculate  $V_{ex}$  using digital elevation data and lithologically varying threshold angles. We constrain the erosion patterns and rates of excess topography using seismic and climate-induced landslides and compiled low-temperature thermochronology data. We then calculate  $T_{ex}$  along and across the mountain range, examine how  $T_{ex}$  varies with slope angles and lithology, and discuss implications for landscape evolution.

# 2. Settings

The Longmen Shan marks the eastern margin of the Tibetan Plateau, featuring a rise of over 5 km within a horizontal distance of 50 km (Burchfiel et al., 2008) (Figure 1a). The regional climate is controlled by the East Asian monsoon, with most precipitation occurring between May and October (Liu-Zeng et al., 2011). This mountain range is seismically active, accommodating the  $2008 \, M_{_W} 7.9$  Wenchuan earthquake (Burchfiel et al., 2008). The

LI ET AL. 2 of 10



bedrock geology is composed of Proterozoic basement granitoid and metamorphic rocks, Paleozoic sequences of metasedimentary rocks and granitic intrusions, Mesozoic sedimentary rocks, and exposures of Cenozoic sediment (Figure 1b) (Burchfiel et al., 2008). Here, the steep topography, active seismicity, and monsoonal climate frequently induce landslides (Li et al., 2017; Parker et al., 2011). Previous studies suggest that this region is a typical threshold landscape, where hillslopes steepen toward a critical angle around  $32-35^{\circ}$  (Ouimet et al., 2009). We chose our study area as a  $300 \times 120$  km window in the central Longmen Shan, overlapping the epicentral region of the Wenchuan earthquake (Figure 1).

# 3. Excess Topography

#### 3.1. Quantification of Excess Topography

We use 30-m-resolution ALOS World 3D Digital Surface Model data (version 3.1. from https://www.eorc.jaxa.jp/ALOS/en/dataset/aw3d30/aw3d30\_e.htm) for topographic analysis. Excess topography is sensitive to threshold angle ( $\theta_0$ ), which varies among lithologies (Blöthe et al., 2015; Korup, 2008). To account for this, we segregate the area into 10 lithologic units (e.g., granite, limestone, sandstone, marble; Ye et al., 2017). For each lithology, we calculate the slope angles of all cells in 3 × 3 moving windows using the "slope" function in ArcGIS and derive its probability distribution. The slope angles of all topographic cells show a near-symmetric distribution with a modal angle ~35° and display distinct patterns across different lithologic units (Figure 2a).

To determine lithology-specific  $\theta_0$ , we first constrain the range of slope angles where the probability of occurrence is greater than 95% of the maximum probability. We consider the minimum and maximum slope angles in this range as the potential lower and upper range of  $\theta_0$  (hereafter,  $\theta_{Llow}$  and  $\theta_{Lup}$ ) and choose the middle point as lithology-specific  $\theta_0$  (hereafter,  $\theta_{L0}$ ).  $\theta_{L0}$  varied from 29° to 39° depending on lithology (Figure S1 in Supporting Information S1). Sedimentary siliciclastic rocks generally have wider distributions of slope angles and lower  $\theta_{L0}$  than other rock types (Figure 2a and Figure S1 in Supporting Information S1).

We calculate excess topography using the "excesstopography" function in MATLAB Topotoolbox2 (Blöthe et al., 2015; Schwanghart & Scherler, 2014; Text S1 in Supporting Information S1). We compute the height  $(Z_{ex})$  and volume  $(V_{ex})$  of excess topography for each of the 10 lithologic units using  $\theta_{L0}$ , with the uncertainties determined from the corresponding  $\theta_{Llow}$  and  $\theta_{Lup}$  (Figures S1 and S2 in Supporting Information S1). We obtain the full-range excess topography by assembling results from each lithology (Figure 1c). We also calculate vertical local relief, as the elevation range within a 1-km-radius circular windows and compare it with  $Z_{ex}$ . One kilometer represents the average planar hillslope length scale in this region (Li et al., 2016).  $V_{ex}$  in the Longmen Shan is  $1,009^{+443}/_{-307}$  km³ and covers  $57^{+9}/_{-8}\%$  of the landscape surface.  $Z_{ex}$  shows heavy-tailed distributions with a median of  $25^{+7}/_{-5}$  m and the median  $Z_{ex}$ -to-vertical-relief ratio is  $2 \pm 1\%$  (Figure S3 in Supporting Information S1).

For simplicity, we group the 10 lithologic units into five primary groups: sedimentary siliciclastic, sedimentary carbonate, granitoid, metasedimentary siliciclastic, and other metamorphic units.

# 3.2. Controls of $\theta_0$ , Slope, and Lithology on Excess Topography

We perform various sensitivity tests to better understand how  $Z_{ex}$  and  $V_{ex}$  vary with  $\theta_0$ , topographic slope, and lithology. First, we calculate  $V_{ex}$  of the whole study area using a uniform  $\theta_0$ , varying from 24° to 41°, which covers the range of  $\theta_{L0}$  from varying lithologic units.  $V_{ex}$  shows >10 times variation with this  $\theta_0$  range, with greater changes in  $V_{ex}$  at lower  $\theta_0$  (Figure 2b). Our estimated  $V_{ex}$  using  $\theta_{L0}$  is similar to  $V_{ex}$  using a fixed  $\theta_0$  of 36.5  $\pm$  2.0°, which is a landscape-scale  $\theta_0$  defined in the same way as in Section 3.1. Despite comparable magnitudes,  $V_{ex}$  is more accurate in local areas when we consider lithologic variations.

Second, we examine how  $Z_{ex}$  varies with slope angles and lithology at local scales. To do this, we segregate our study area into 1,440 grids of a 5 × 5 km size and calculate mean  $Z_{ex}$  and mean slope angles of all cells in each grid (hereafter, grid  $Z_{ex}$  and grid slope).  $Z_{ex}$  increases with grid slope angles (Figure S4a in Supporting Information S1), which is expected because the steeper hillslopes can accommodate higher heights of rock columns above  $\theta_0$  (Blöthe et al., 2015).

LI ET AL. 3 of 10



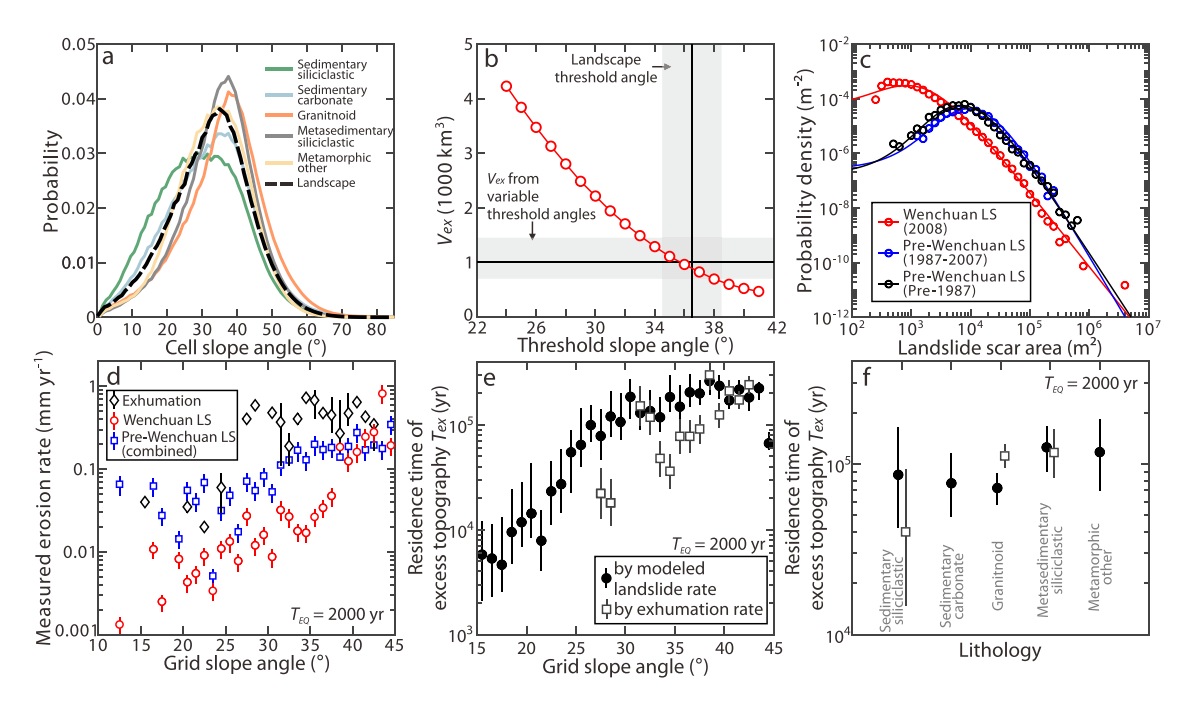


Figure 2. Characterization of slope, erosion rate, excess topography, and  $T_{ex}$ . (a) Cell slope angle distributions for different lithologies and the landscape; (b) threshold slope angle  $\theta_0$  versus  $V_{ex}$  calculated using a uniform  $\theta_0$  (red circles) and  $V_{ex}$  based on  $\theta_{L0}$  (horizontal solid line) and  $\theta_0$  from the full landscape (vertical solid line) and their uncertainties from lower-and-upper bounds of  $\theta_0$  (shaded areas); (c) landslide-scar area versus probability density with the inverse-gamma fits for the Wenchuan, pre-1987, and 1987–2007 inventories (Table S3 in Supporting Information S1); (d) grid landslide erosion and exhumation rates versus grid slope angle, reported as the medians (symbols) and 16th–84th percentiles (error bars) for rate data grouped by 1° grid slope bins;  $T_{ex}$  varying with (e) grid slope angle, and (f) lithology. In (e and f), we first calculate landslide-derived  $T_{ex}$  for each grid as the median of Monte Carlo simulations using  $\theta_{L0}$  and  $T_{EQ}$  of 2,000 years. Grid  $T_{ex}$  are grouped by grid slope angle in 1° slope bins and by the dominant lithology of the grid. We report the medians of grid landslide-derived  $T_{ex}$  (filled circles) and grid exhumation-derived  $T_{ex}$  (empty squares) in each slope bin and in each lithologic group using  $\theta_{L0}$  (error bars from  $\theta_{Lloy}$  and  $\theta_{Lup}$ ).

Third, we calculate mean  $Z_{ex}$  from the grids grouped by dominant lithology of the highest areal proportion. For  $Z_{ex}$  defined by  $\theta_{L0}$  (Figure S5a in Supporting Information S1), mean  $Z_{ex}$  is slightly higher in granitoid rocks and is comparable across other rocks. Mean  $Z_{ex}$  defined by  $\theta_{Lup}$  and  $\theta_{Llow}$  tend to have wider ranges in certain rock types (e.g., sedimentary siliciclastic rocks). The variations are likely caused by the wide probability distributions of slope angles (Figure 2a), which result in large ranges of  $\theta_{Lup}$  and  $\theta_{Llow}$ . However, mean  $Z_{ex}$  are generally comparable across different lithologies, likely due to the combination of vertical relief and the proportion of steeper-than- $\theta_{L0}$  cells (Figure S5b in Supporting Information S1).

Lastly, the observed slope and lithologic controls explain the spatial patterns of  $Z_{ex}$ .  $Z_{ex}$  increases in the frontal mountains and saturates toward hinterlands (A–A', Figure 1f), mirroring the changes in slope angles. Along the mountain range (B–B', Figure 1j), slope angles do not vary much, but  $Z_{ex}$  and lithologies have greater variations. We attribute the variations in  $Z_{ex}$  along B–B' to changes in lithologic compositions (Figure S2 in Supporting Information S1).

# 4. Long-Term Erosion Rates

Landslides likely dominate erosional processes in over-steepened slopes in the Longmen Shan (Li et al., 2017; Ouimet et al., 2009). Here, we constrain the long-term landslide erosion rates (rates of new landslide generation) from present-day landslide inventories and modeling over multiple earthquake-cycle time scales. Then, we constrain long-term exhumation rates by compiling low-temperature thermochronology data.

#### 4.1. Landslide Characteristics, Distribution, and Erosion Patterns

#### 4.1.1. Landslide Inventories and Landslide Size Distribution

We use an existing Wenchuan earthquake-triggered landslide inventory map (Li et al., 2014, 2016) and prepare two new pre-Wenchuan landslide inventory maps. The pre-Wenchuan landslides are mapped from 30-m-resolu-

LI ET AL. 4 of 10



tion Landsat images for 1987–2007 (642 landslides for the 1987–2007 inventory) and 1986 (3,070 landslides for the pre-1987 inventory; Figure 1d and Table S1 in Supporting Information S1). The pre-1987 and 1987–2007 inventories represent periods with no major seismicity in the area (Densmore et al., 2007). Thus, we attribute those landslides to be induced by climatic factors (e.g., rainstorms and flooding).

Landslides are identified based on the contrasting brightness between landslide-affected areas and surrounding vegetation through visual examination and are manually mapped as polygons including both scar and deposition zones. We estimate scar area adopting the methods proposed by Marc et al. (2018). For each landslide polygon, we compute a mean landslide width (W) and a length-to-width ratio from the measured planar area and perimeter assuming an ellipse shape (Marc & Hovius, 2015). Based on a locally measured scar length-to-width ratio of 2.5, we calculate scar area as  $A_S = 2.5W^2$ . The scar areas are converted to volumes ( $V_{LS}$ ) using a group of published area-volume scaling relations (Table S2 in Supporting Information S1; Li et al., 2014). Details about landslide mapping and scar volume estimation are explained in Text S2 in Supporting Information S1.

To characterize landslide size distributions, we fit all three landslide inventories to a three-parameter inverse-gamma function using a maximum likelihood estimation approach (Figure 2c and Text S2 in Supporting Information S1; Malamud et al., 2004; Marc et al., 2019). The pre-1987 and 1987–2007 inventories have similar distributions, which suggest similar triggering mechanisms and corroborate our treatment of both inventories as climate-induced (e.g., Larsen & Montgomery, 2012; Malamud et al., 2004; Marc et al., 2015). The function features a power-law relation between probability density  $p(A_s)$  and landslide-scar area  $A_s$  as  $p(A_s) \sim A_s^{-(\rho+1)}$ . The Wenchuan inventory has a power-law tail ( $\rho + 1 = 2.72$ , Table S3 in Supporting Information S1) shallower than the pre-Wenchuan inventories (3.33 and 3.70 for the pre-1987 and 1987–2007 inventories, respectively), meaning that seismic landslides have a higher abundance of large sizes than climate-induced landslides. This result is consistent with observations from landslides in Nepal, although those seismically and climatically induced landslides have shallow and close power-law tails ( $\rho + 1 = 2.23-2.43$  versus 2.5, respectively; Marc et al., 2019).

#### 4.1.2. Landslide Occurrences Across Slopes

The modal slope angles of landscape cells affected by the Wenchuan and pre-Wenchuan landslides are  $\sim$ 42° and  $\sim$ 38°, respectively, slightly steeper than that of all landscape cells ( $\sim$ 35°; Figure S5c in Supporting Information S1). To characterize landslide propensity across slopes, we calculate the probability ratios—the ratios between the slope probability distributions of landslide-affected cells and landscape cells—for the Wenchuan and pre-Wenchuan landslides (Marc et al., 2018; Rault et al., 2019; Text S3 in Supporting Information S1). The slopes affected by the Wenchuan and pre-Wenchuan landslide cells are statistically different from random samplings of landscapes (Figures S5d and S5e in Supporting Information S1). For slopes >40°, the probability ratio for the Wenchuan landslides is greater than that of pre-Wenchuan landslides, suggesting a higher propensity of seismic landslides than climate-induced landslides in those steep slopes. The mapped landslides mostly occur in excess topography, with <5% (by volume) occurring in slopes shallower than  $\theta_{L0}$  (Figure S5f in Supporting Information S1).

#### 4.1.3. Landslide Erosion Patterns

To examine how landslide erosion varies across landscapes, we measure landslide rates in the  $5 \times 5$  km grids. To do this, we sum the volumes of mapped landslides in the grid and then normalize it by the timespan of the mapped landslides ( $T_{map}$ ) and grid area ( $25 \text{ km}^2$ ) for each inventory.  $T_{map}$  for the Wenchuan landslide inventory is the recurrence interval of the Wenchuan earthquake event ( $T_{EQ}$ ), which is estimated to be 500–4,000 years (Li et al., 2017). Here, we take a reference  $T_{EQ}$  of 2,000 years.  $T_{map}$  for the 1987–2007 inventory is 20 years, the timespan of the mapped images. Assuming the pre-1987 landslides occurred at the same rate as the 1987–2007 landslides, we estimate a  $T_{map}$  of 72 years for pre-1987 inventory. We term the landslide rates calculated here "measured landslide rates" to distinguish from the "modeled long-term landslide rates" introduced in Section 4.2.

We group the measured landslide rates by grid slope angles in  $1^{\circ}$  slope bins and compare the medians of landslide rates in each slope bin against grid slope angles (Figure 2d). Both Wenchuan and pre-Wenchuan measured landslide rates generally increase with grid slope angles, with the Wenchuan landslide rates increasing faster than the pre-Wenchuan rates at  $>35^{\circ}$  slopes. These observations indicate that gentle-to-steep slopes ( $20-35^{\circ}$ ) are eroded by both seismic and climate-induced landslides, but very steep slopes ( $>40^{\circ}$ ) are dominantly eroded by seismic landslides. The observed high seismic landslides rates in steep slopes are likely due to the amplification of shaking (e.g., at ridges) during earthquakes (Meunier et al., 2008; Rault et al., 2019). The measured landslide rates are highest in granitoid rocks across different lithologies (Figure S5h in Supporting Information S1).

LI ET AL. 5 of 10



#### 4.2. From Modern Landsliding to Long-Term Erosion

#### 4.2.1. Long-Term Seismic and Climate-Induced Landslide Rates for the Entire Study Area

The measured landslide rates do not represent long-term landslide rates because they do not include landslides caused by earthquakes with magnitudes different from the Wenchuan event and the mapped inventories may be incomplete (e.g., Malamud et al., 2004). Here, we explain how we use modeling approaches to estimate long-term landslide erosion rates and their uncertainties over multiple earthquake-cycle time scales (~10s kyr).

We model total  $V_{LS}$  over multiple earthquake cycles and calculate long-term seismic landslide rates following the methods presented in Li et al. (2017). We provide a summary of the methods in Li et al. (2017) that we adopted here and more details in Text S4 in Supporting Information S1. First, Li et al. (2017) derive empirical relationships between local peak ground accelerations (PGA) and  $V_{IS}$  using the Wenchuan landslide data. Second, for other earthquake events with no landslide data, Li et al. (2017) predict PGA spectra from a calibrated Ground Motion Prediction Equation and use the predicted PGA to estimate local landslide volumes from the Wenchuan  $PGA - V_{LS}$  relationships. The local volumes are summed for a total  $V_{LS}$ . Using this approach, Li et al. (2017) model  $V_{LS}$  for 20 events from  $M_w \sim 5$  to 8 and fit an empirical  $M_w - V_{LS}$  relation.  $M_w \sim 5$  is thought to be the minimum magnitude to trigger landslides (Marc et al., 2016).  $M_w \sim 8$  likely represents the maximum magnitude in the region, because the Wenchuan earthquake almost ruptured the full length of the fault system (Lin et al., 2016; Liu-Zeng et al., 2009). Third, Li et al. (2017) calibrates regional  $M_w$ -frequency relationships and define empirical relationships between  $M_w$  and the probability of shallow, landslide-triggering events using instrumental and paleoseismic data. Lastly, Li et al. (2017) integrate the  $M_w - V_{LS}$  fit based on  $M_w$ -frequency and  $M_w$ -landslide-triggering probability relationships over  $M_w \sim 5$ –8 for 1,000 Wenchuan earthquake cycles. This method calculates longterm seismic landslide volumes and their uncertainties from the residual  $(\varepsilon_r)$  of the  $M_w - V_{LS}$  fit (Li et al., 2017, Text S4 in Supporting Information S1).

We then adjust the landslide volumes to account for the potential incompleteness of the mapped inventories. To do this, we integrate  $V_{LS}$  over the fitted inverse-gamma function that describes the size-frequency distribution of the corresponding inventory following methods from previous studies (Hovius et al., 1997; Malamud et al., 2004; Marc et al., 2019). The integration is done from the smallest scar area in each inventory to the maximum scar area of all three inventories ( $\sim$ 4 km²). We obtain a correction factor determined from the integrated  $V_{LS}$  over the fitted inverse-gamma function. Then, we multiply the modeled long-term seismic landslide volumes over multiple earthquake cycles with the correction factor. The corrected  $V_{LS}$  is normalized by  $A_{map}$  (36,000 km²) and the integration timespan (1,000 ×  $T_{EO}$ ) to obtain long-term seismic landslide rates.

For climate-induced landslides, we normalize the integrated  $V_{LS}$  from the 1987 to 2007 inventory by mapped area  $(A_{map}, 36,000 \text{ km}^2)$  and timespan  $(T_{map}, 20 \text{ years})$  to obtain climate-induced landslide rates for the study area.

Then, we obtain total long-term landslide rates by summing the modeled seismic landslide rates and climate-induced landslide rates. The long-term landslide rates are calculated using different  $T_{EQ}$  values across its estimated range of 500–4,000 years. We also estimate the uncertainties of modeled landslide rates using a Monte Carlo simulation through 1,000,000 random samplings to account for the variations in landslide area-volume scaling parameters and  $M_w - V_{LS}$  scaling (Text S5 in Supporting Information S1).

We report the long-term landslide erosion rates and uncertainties as the medians and 16th–84th percentiles of the Monte Carlo simulation results, respectively. Our modeled long-term landslide fluxes are  $9.1^{+2.9}/_{-2.1}-11.9^{+3.0}$   $9/_{-3.0}\times10^{-3}~\rm km^3~\rm yr^{-1}$  over  $A_{map}$  across the range of  $T_{EQ}$ , equivalent to landslide erosion rates of  $0.25^{+0.08}/_{-0.06}-0.34^{+0.11}/_{-0.08}~\rm mm~\rm yr^{-1}$ . The corresponding seismic and climate-induced landslide rates are  $0.11^{+0.04}/_{-0.03}-0.19^{+0.00}/_{-0.04}$  mm yr<sup>-1</sup> and  $0.15^{+0.04}/_{-0.03}~\rm mm~\rm yr^{-1}$ , respectively.

Our modeled climate-induced landslide fluxes are comparable to seismic landslide fluxes in the Longmen Shan, similar to findings in the Himalayas (Marc et al., 2019). Based on the Wenchuan and pre-Wenchuan landslide data (Figures 1g and 1k), seismic landslides mainly occur and dominate landslide budgets in frontal mountains where seismogenic faults are located, whereas climate-induced landslides occur more evenly across the range and dominate in the interior mountains.

We acknowledge that our measurements for seismic and climate-induced landslide fluxes may not be complete and have some uncertainties. First, we do not model landslides in the interior mountains triggered by seismicity in adjacent fault systems (e.g., Minjiang and Huya faults; Hu et al., 2012). Second, it is possible that we miss

LI ET AL. 6 of 10



some landslides in areas with minimal vegetation cover (e.g., high elevation) or due to low-resolution images. Particularly, the images for mapping the pre-Wenchuan landslides have a lower resolution (30 m) than those for the Wenchuan landslides (10 m; Li et al., 2014). Considering possible size distributions for unmapped small landslides in pre-Wenchuan inventories, we suggest that the underestimated climate-induced landslide volumes can be up to 8% (Text S2 in Supporting Information S1).

#### 4.2.2. Long-Term Erosion Rates for $5 \times 5$ km Grids

To constrain long-term erosion rates and quantify  $T_{ex}$  across landscapes, we model landslide rates in the 5 × 5 km grids using an algorithm to distribute landslide volumes within the grids (Text S5, Figure S6, and Table S4 in Supporting Information S1). In short, this algorithm first calculates the differences between the volume of the mapped landslides and the modeled long-term  $V_{LS}$  that accounts for (a) the landslides triggered by  $M_w < 8$  earth-quakes and (b) the potential incompleteness of the mapped inventories. Then, the algorithm randomly distributes the differential volume from entire region into each grid cell and generates long-term  $V_{LS}^*$  for each grid.

For each grid, the three long-term  $V_{LS}$  are normalized by an  $A_{map}$  of 25 km² and corresponding  $T_{map}$  to convert to landslide rates. In each grid, we take the average of the landslide rates derived from the 1987–2007 and pre-1987 inventories as a combined climate-induced landslide rate and add it to the modeled seismic landslide rate in that grid. We model the distributions of long-term  $V_{LS}^*$  for the Wenchuan, pre-1987, and 1987–2007 inventories separately using a reference  $T_{EO}$  of 2,000 years. The results of each grid are then used for estimating grid  $T_{ex}$ .

#### 4.3. Exhumation Rates From Low-Temperature Thermochronology

We adopt exhumation rate data from Tian et al. (2013). They compiled a low-temperature thermochronology data set, which includes apatite and zircon (U-Th)/He ages, apatite fission track, and zircon fission track in the region, and modeled averaged exhumation rates over million-year time scales (hereafter, exhumation rates). The compiled exhumation rates vary from 0.02 to 2.80 mm yr<sup>-1</sup>, with an average of  $0.41 \pm 0.35$  mm yr<sup>-1</sup> (mean  $\pm 1\sigma$ , n = 110) for the entire region (Tian et al., 2013), which is comparable to our estimated long-term landslide erosion rates. We calculate mean exhumation rates for the  $5 \times 5$  km grids for which have  $\geq 3$  data points. Because we focus on erosion of rock masses within excess topography, we exclude data points sampled outside excess topography. This removes ~70 data points in the compilation but does not cause significant changes to the average exhumation rate (detailed statistics in Text S6 of Supporting Information S1). The mean grid exhumation rates show a generally positive, although scattered, trend with grid slope angles, increasing rapidly from 25° to 30–40° (Figure 2d). This pattern is similar to the trends observed in the measured landslide erosion rates in this study and in the exhumation rate data in other regions (Montgomery & Brandon, 2002). The mean grid exhumation rates are comparable across three dominant lithologies (Figure S5h in Supporting Information S1).

# 5. Residence Time of Rock Masses in Excess Topography

#### 5.1. Calculation of the Residence Time

We calculate  $T_{ex}$  at the range-scale and in the  $5 \times 5$  km grids and estimated their uncertainties (Text S5 and Figure S6 in Supporting Information S1). We normalize the total  $V_{ex}$  for range-scale and grid-scale  $T_{ex}$  by the extent of the study area  $(A_{ex})$  of 36,000 and 25 km², respectively. We use e from the modeled long-term landslide erosion rates and the compiled exhumation rates to calculate landslide-derived and exhumation-derived  $T_{ex}$ , respectively. As described in earlier sections, the estimates and uncertainties of  $T_{ex}$  are affected by the choice of (a) threshold angles that determine the volume of excess topography and (b) landslide-related factors that affect long-term landslide erosion rates.

We calculate  $T_{ex}$  for different threshold angle scenarios ( $\theta_{L0}$ ,  $\theta_{Llow}$ ,  $\theta_{Lup}$ ) across the range. For landslide-derived  $T_{ex}$  we calculate  $T_{ex}$  for given threshold angle conditions and  $T_{EQ}$  then use a Monte Carlo random sampling approach to quantify uncertainty of  $T_{ex}$  sourced from the landslide-related factors (Text S5 in Supporting Information S1). The uncertainties of  $T_{ex}$  from our Monte Carlo simulation are on the same order of magnitude as those from  $\theta_0$  (Figure S7a in Supporting Information S1). For simplicity, we report  $T_{ex}$  as the median value of the Monte Carlo simulation using  $\theta_{L0}$  and the uncertainties of  $T_{ex}$  as the ranges of the median values from  $\theta_{Llow}$  and  $\theta_{Lup}$ .

LI ET AL. 7 of 10



Using modeled long-term landslide erosion rates and exhumation rates, we estimate a range-scale  $T_{ex}$  of 61–157 kyr (encompassing  $T_{ex}$  of 87<sup>+38</sup>/ $_{-26}$  – 109<sup>+48</sup>/ $_{-33}$  kyr across the range of  $T_{EQ}$ . Figure S7a in Supporting Information S1) and of 62<sup>+17</sup>/ $_{-19}$  kyr, respectively.

#### 5.2. Patterns and Controls of Residence Time

We hypothesize that  $T_{ex}$  is controlled by slope angles and lithology as these two factors affect excess topography and erosion rates (Figures 2e, 2f and Figure S4 in Supporting Information S1). To examine this, we compare  $T_{ex}$  from grids with varying grid slope angles and lithologies. Indeed, in landscapes with grid slope angles >15° (that compose >99% of total excess topography, Figure S4b in Supporting Information S1), the landslide-derived  $T_{ex}$  increases with mean grid angle from ~15° to 30° and saturates at steeper angles (Figure 2e). The increasing trend reveals a faster growth of excess topography than landslide rates in shallow slopes. The saturation is likely due to the commensurate increase of landslide rates in response to the increase of excess topography as slopes steepen. Exhumation-derived  $T_{ex}$  shows a similar general trend to the landslide-derived  $T_{ex}$  but is more scattered at angles >30°. The differences are likely caused by heterogeneities of the exhumation rate data and nonlandslide erosion captured by exhumation rates.

Nonetheless, our analysis suggests that rock masses on steeper slopes can reside for longer time periods (>10 times) than on shallower slopes. Our calculated  $T_{ex}$  from landslide rates have minor differences across lithologies. Metamorphic rocks have a  $T_{ex}$  slightly longer (<~2 times) than that of sedimentary and granitoid rocks. Although  $Z_{ex}$  is slightly higher in granitoid rocks under  $\theta_{L0}$ , the corresponding  $T_{ex}$  is shorter than other rock types. This is likely because of high erosion rates in granitoid rocks which have steep slopes and are located in mountain fronts where intense weathering and fault damage occur (Kirkpatrick et al., 2021; Li & Moon, 2021). Exhumation-derived  $T_{ex}$  for different lithologies where data are sufficient are consistent with those derived from landslide rates, except for granitoid rocks (Figure 2f). This is likely because most exhumation rate data are sampled from areas with very steep slopes (34–43°) where  $T_{ex}$  is high.

The controls from slope angle and lithology on  $T_{ex}$  explain the spatial patterns of  $T_{ex}$  across and along the Longmen Shan. Landslide-derived  $T_{ex}$  follows the variation of slope angle across the mountain range and lithologies along the mountain range. For a reference  $T_{EQ}$  of 2,000 years,  $T_{ex}$  increases by a factor of 5 (30–150 kyr) from the range front to the hinterland (Figure 1h). Along the mountain front range,  $T_{ex}$  fluctuates within a factor of  $\sim$ 3 (Figure 1l). Lower  $T_{ex}$  values in the southern segment than those in the northern segment correspond to greater proportions of sedimentary siliciclastic and granitoid rocks and higher local erosion rates (Figure S2 in Supporting Information S1).  $T_{ex}$  from other  $T_{EQ}$  shows similar trends and magnitudes of changes (Figures S8 and S9 in Supporting Information S1). Exhumation-derived  $T_{ex}$  has consistent patterns with landslide-derived  $T_{ex}$  (Figures 1h and 1l).

#### 5.3. Implications

We compare  $T_{ex}$  to the time scale of topographic relief rejuvenation, the ratio between an average hillslope-scale relief and a long-term uplift rate. Considering an average hillslope relief of ~700 m in the region and using a range-scale average exhumation rate of 0.41 mm yr<sup>-1</sup> to approximate the long-term rock uplift rate, we estimate the rejuvenation time scale of topographic relief as ~1,700 kyr. Our estimated  $T_{ex}$  of ~61–157 kyr suggests that hillslopes already at or nearing threshold angles can continue steepening for ~3–9% of the relief-rejuvenation timespan.  $T_{ex}$  also bounds the time length of geochemical reactions on landslide-prone hillslopes, providing useful constraints for hillslope-weathering models (e.g., West, 2012). Similar  $T_{ex}$  from varying lithologies and different erosion rate measurement methods suggest that the Longmen Shan may maintain steady-state construction and erosion of excess topography over kyr-to-Myr time scales.

# 6. Conclusions

We quantify the residence time of rock masses in excess topography in eastern Tibetan mountains. Our work shows that the height of excess topography and long-term erosion rates covary with slope and lithology, which produce  $T_{ex}$  within the same order of magnitude across different lithologies. We estimate a mountain-scale  $T_{ex}$  of  $\sim$ 61–157 kyr using modeled long-term landslide rates, and the lower bound of the range is comparable to the  $T_{ex}$ 

LI ET AL. 8 of 10



( $\sim$ 62 kyr) derived from exhumation rates.  $T_{ex}$  is longer for rock masses on steeper slopes and is of the similar order of magnitude across lithologies, with times slightly longer for metamorphic rocks.  $T_{ex}$  increases by a factor of  $\sim$ 5 across the mountain range, following changes in slope angles, and fluctuates by a factor of  $\sim$ 3 along the range, covarying with the changes in local lithology and erosion rates. Overall, our work provides methods that can be used to characterize  $T_{ex}$  in other mountains, and our findings provide new insights into the evolution time scales of landscapes beyond threshold angles.

# **Data Availability Statement**

The Wenchuan landslide data are available from the USGS data repository (https://doi.org/10.5066/F7H70DB4). The pre-Wenchuan landslide data are archived at HydroShare Data Repository (http://www.hydroshare.org/resource/36639c83d43644d79be80828f6487ab0).

#### Acknowledgments

This work was supported by NSF EAR-1945431. The authors thank Douglas Madison and Kevin Shao for helpful discussions. The authors thank Odin Marc, Jan Blöthe, and an anonymous reviewer for their constructive comments and Lucy Flesch for editorial handling.

#### References

- Bennett, G. L., Miller, S. R., Roering, J. J., & Schmidt, D. A. (2016). Landslides, threshold slopes, and the survival of relict terrain in the wake of the Mendocino Triple Junction. *Geology*, 44(5), 363–366. https://doi.org/10.1130/g37530.1
- Blöthe, J. H., Korup, O., & Schwanghart, W. (2015). Large landslides lie low: Excess topography in the Himalaya-Karakoram ranges. *Geology*, 43(6), 523–526. https://doi.org/10.1130/g36527.1
- Bolin, B., & Rodhe, H. (1973). A note on the concepts of age distribution and transit time in natural reservoirs. *Tellus*, 25(1), 58–62. https://doi.org/10.3402/tellusa.v25i1.9644
- Burbank, D., Leland, J., Fielding, E., Anderson, R. S., Brozovic, N., Reid, M. R., & Duncan, C. (1996). Bedrock incision, rock uplift and threshold hillslopes in the northwestern Himalayas. *Nature*, 379, 505–510. https://doi.org/10.1038/379505a0
- Burchfiel, B. C., Royden, L. H., van der Hilst, R. D., Hager, B. H., Chen, Z., King, R. W., et al. (2008). A geological and geophysical context for the Wenchuan earthquake of 12 May 2008, Sichuan, People's Republic of China. *Geological Society of America Today*, 18(7), 5. https://doi.org/10.1130/gsatg18a.1
- Croissant, T., Hilton, R. G., Li, G. K., Howarth, J., Wang, J., Harvey, E. L., et al. (2021). Pulsed carbon export from mountains by earthquake-triggered landslides explored in a reduced-complexity model. *Earth Surface Dynamics*, 9(4), 823–844. https://doi.org/10.5194/esurf-9-823-2021
- Densmore, A. L., Ellis, M. A., Li, Y., Zhou, R. J., Hancock, G. S., & Richardson, N. (2007). Active tectonics of the Beichuan and Pengguan faults at the eastern margin of the Tibetan Plateau. *Tectonics*, 26, TC4005. https://doi.org/10.1029/2006TC001987
- Emberson, R., Hovius, N., Galy, A., & Marc, O. (2016). Chemical weathering in active mountain belts controlled by stochastic bedrock landsliding. *Nature Geoscience*, 9(1), 42–45. https://doi.org/10.1038/ngeo2600
- Hovius, N., Stark, C. P., & Allen, P. A. (1997). Sediment flux from a mountain belt derived by landslide mapping. *Geology*, 25, 231–234. https://doi.org/10.1130/0091-7613(1997)025<0231:sffamb>2.3.co;2
- Hu, C., Cai, Y., & Wang, Z. (2012). Effects of large historical earthquakes, viscous relaxation, and tectonic loading on the 2008 Wenchuan earthquake. Journal of Geophysical Research, 117, B06410. https://doi.org/10.1029/2011JB009046
- Kirby, E., Whipple, K. X., Tang, W., & Chen, Z. (2003). Distribution of active rock uplift along the eastern margin of the Tibetan Plateau: Inferences from bedrock channel longitudinal profiles. *Journal of Geophysical Research*, 108(B4), 2217. https://doi.org/10.1029/2001JB000861
- Kirkpatrick, H. M., Moon, S., Yin, A., & Harrison, T. M. (2021). Impact of fault damage on eastern Tibet topography. *Geology*, 49(1), 30–34. https://doi.org/10.1130/g48179.1
- Korup, O. (2008). Rock type leaves topographic signature in landslide-dominated mountain ranges. Geophysical Research Letters, 35, L11402. https://doi.org/10.1029/2008GL034157
- Korup, O., Clague, J. J., Hermanns, R. L., Hewitt, K., Strom, A. L., & Weidinger, J. T. (2007). Giant landslides, topography, and erosion. Earth and Planetary Science Letters, 261, 578–589. https://doi.org/10.1016/j.epsl.2007.07.025
- Larsen, I. J., & Montgomery, D. R. (2012). Landslide erosion coupled to tectonics and river incision. Nature Geoscience, 5(7), 468–473. https://doi.org/10.1038/ngeo1479
- Li, G., West, A. J., Densmore, A. L., Hammond, D. E., Jin, Z., Zhang, F., et al. (2016). Connectivity of earthquake-triggered landslides with the fluvial network: Implications for landslide sediment transport after the 2008 Wenchuan earthquake. *Journal of Geophysical Research: Earth Surface*, 121, 703–724. https://doi.org/10.1002/2015JF003718
- Li, G., West, A. J., Densmore, A. L., Jin, Z., Parker, R. N., & Hilton, R. G. (2014). Seismic mountain building: Landslides associated with the 2008 Wenchuan earthquake in the context of a generalized model for earthquake volume balance. *Geochemistry, Geophysics, Geosystems*, 15, 833–844. https://doi.org/10.1002/2013GC005067
- Li, G., West, A. J., Densmore, A. L., Jin, Z., Zhang, F., Wang, J., et al. (2017). Earthquakes drive focused denudation along a tectonically active mountain front. Earth and Planetary Science Letters, 472, 253–265. https://doi.org/10.1016/j.epsl.2017.04.040
- Li, G. K., & Moon, S. (2021). Topographic stress control on bedrock landslide size. Nature Geoscience, 14(5), 307–313. https://doi.org/10.1038/s41561-021-00739-8
- Lin, A., Yan, B., & Rao, G. (2016). Millennium recurrence interval of morphogenic earthquakes on the Qingchuan fault, northeastern segment of the Longmen Shan Thrust Belt, China. *Journal of Seismology*, 20(2), 535–553. https://doi.org/10.1007/s10950-015-9542-8
- Liu-Zeng, J., Wen, L., Oskin, M., & Zeng, L. S. (2011). Focused modern denudation of the Longmen Shan margin, eastern Tibetan Plateau. Geochemistry, Geophysics, Geosystems, 12, Q11007. https://doi.org/10.1029/2011GC003652
- Liu-Zeng, J., Zhang, Z., Wen, L., Tapponnier, P., Sun, J., Xing, X., et al. (2009). Co-seismic ruptures of the 12 May 2008, Ms 8.0 Wenchuan earthquake, Sichuan: East-west crustal shortening on oblique, parallel thrusts along the eastern edge of Tibet. Earth and Planetary Science Letters, 286(3), 355–370. https://doi.org/10.1016/j.epsl.2009.07.017
- Malamud, B. D., Turcotte, D. L., Guzzetti, F., & Reichenbach, P. (2004). Landslides, earthquakes, and erosion. Earth Planetary Sciencee Letters, 229(1–2), 45–59.

LI ET AL. 9 of 10



- Marc, O., Behling, R., Andermann, C., Turowski, J. M., Illien, L., Roessner, S., & Hovius, N. (2019). Long-term erosion of the Nepal Himalayas by bedrock landsliding: The role of monsoons, earthquakes and giant landslides. *Earth Surface Dynamics*, 7(1), 107–128. https://doi.org/10.5194/esurf-7-107-2019
- Marc, O., & Hovius, N. (2015). Amalgamation in landslide maps: Effects and automatic detection. *Natural Hazards and Earth System Sciences*, 15(4), 723–733. https://doi.org/10.5194/nhess-15-723-2015
- Marc, O., Hovius, N., Meunier, P., Gorum, T., & Uchida, T. (2016). A seismologically consistent expression for the total area and volume of earthquake-triggered landsliding. *Journal of Geophysical Research: Earth Surface*, 121, 640–663. https://doi.org/10.1002/2015JF003732
- Marc, O., Hovius, N., Meunier, P., Uchida, T., & Hayashi, S. (2015). Transient changes of landslide rates after earthquakes. *Geology*, 43(10), 883–886. https://doi.org/10.1130/g36961.1
- Marc, O., Stumpf, A., Malet, J. P., Gosset, M., Uchida, T., & Chiang, S. H. (2018). Initial insights from a global database of rainfall-induced landslide inventories: The weak influence of slope and strong influence of total storm rainfall. *Earth Surface Dynamics*, 6(4), 903–922. https://doi.org/10.5194/esurf-6-903-2018
- Meunier, P., Hovius, N., & Haines, J. A. (2008). Topographic site effects and the location of earthquake induced landslides. Earth and Planetary Science Letters, 275(3–4), 221–232. https://doi.org/10.1016/j.epsl.2008.07.020
- Montgomery, D. R. (2001). Slope distributions, threshold hillslopes, and steady-state topography. *American Journal of Science*, 301(4–5), 432–454. https://doi.org/10.2475/ajs.301.4-5.432
- Montgomery, D. R., & Brandon, M. T. (2002). Topographic controls on erosion rates in tectonically active mountain ranges. Earth and Planetary Science Letters, 201(3-4), 481–489. https://doi.org/10.1016/s0012-821x(02)00725-2
- Ouimet, W. B., Whipple, K. X., & Granger, D. E. (2009). Beyond threshold hillslopes: Channel adjustment to base-level fall in tectonically active mountain ranges. *Geology*, 37(7), 579–582. https://doi.org/10.1130/g30013a.1
- Parker, R. N., Densmore, A. L., Rosser, N. J., de Michele, M., Li, Y., Huang, R. Q., et al. (2011). Mass wasting triggered by the 2008 Wenchuan earthquake is greater than orogenic growth. *Nature Geoscience*, 4(7), 449–452. https://doi.org/10.1038/ngeo1154
- Rault, C., Robert, A., Marc, O., Hovius, N., & Meunier, P. (2019). Seismic and geologic controls on spatial clustering of landslides in three large earthquakes. *Earth Surface Dynamics*, 7(3), 829–839.
- Schwanghart, W., & Scherler, D. (2014). Short communication: TopoToolbox 2—MATLAB-based software for topographic analysis and modeling in Earth surface sciences. Earth Surface Dynamics, 2(1), 1–7. https://doi.org/10.5194/esurf-2-1-2014
- Tian, Y., Kohn, B. P., Gleadow, A. J. W., & Hu, S. (2013). Constructing the Longmen Shan eastern Tibetan Plateau margin: Insights from low-temperature thermochronology. *Tectonics*, 32, 576–592. https://doi.org/10.1002/tect.20043
- West, A. J. (2012). Thickness of the chemical weathering zone and implications for erosional and climatic drivers of weathering and for carbon-cycle feedbacks. *Geology*, 40(9), 811–814. https://doi.org/10.1130/g33041.1
- Whipple, K., Kirby, E., & Brocklehurst, S. (1999). Geomorphic limits to climate-induced increases in topographic relief. *Nature*, 401, 39–43. https://doi.org/10.1038/43375
- Ye, T., Huang, C., & Deng, Z. (2017). Spatial database of 1:2500000 digital geologic map of People's Republic of China. *Geology in China*, 44(S1), 19–24

# **References From the Supporting Information**

- An, Z., Wu, G., Li, J., Sun, Y., Liu, Y., Zhou, W., et al. (2015). Global monsoon dynamics and climate change. *Annual Review of Earth and Planetary Sciences*, 43(1), 29–77.
- Guzzetti, F., Ardizzone, F., Cardinali, M., Rossi, M., & Valigi, D. (2009). Landslide volumes and landslide mobilization rates in Umbria, central Italy. Earth and Planetary Science Letters, 279, 222–229.
- Larsen, I. J., Montgomery, D. R., & Korup, O. (2010). Landslide erosion controlled by hillslope material. Nature Geoscience, 3(4), 247-251.
- Lee, S., & Talib, J. A. (2005). Probabilistic landslide susceptibility and factor effect analysis. Environmental Geology, 47(7), 982–990.
- Milledge, D. G., Densmore, A. L., Bellugi, D., Rosser, N. J., Watt, J., Li, G., & Oven, K. J. (2019). Simple rules to minimise exposure to coseismic landslide hazard. *Natural Hazards and Earth System Sciences*, 19(4), 837–856.
- Perron, J. T. (2017). Climate and the pace of erosional landscape evolution. Annual Review of Earth and Planetary Sciences, 45(1), 561-591.

LI ET AL. 10 of 10